Science

AAAS

Supplementary Materials for

Self-sustaining personal all-day thermoregulatory clothing using only sunlight

Ziyuan Wang *et al*.

Corresponding authors: Yongsheng Liu, liuys@nankai.edu.cn; Rujun Ma, malab@nankai.edu.cn; Yongsheng Chen, yschen99@nankai.edu.cn

The PDF file includes:

Other Supplementary Material for this manuscript includes the following:

Content

Materials and Methods

Preparation of the flexible large-area OPV module

Preparation of the flexible heat transfer layer

Preparation of the flexible EC device

Preparation of the perovskite solar module

Preparation of the artificial skin

Fabrication of the OETC system

Characterization of the OPV module

Comparison of the EC device driven by OPV module and electric supply

Calculation of the average heat flux and power consumption

Supplementary Text

Calculation of the required OPV module area to provide all-day thermoregulation for individual space travel

Definition of Cu-PE, TiO$_2$/PLA/PTFE, NFM, Janus film and NanoPE in Fig. 3F

Supplementary Figures

1. Preparation of the flexible large-area OPV module
2. J-V curve of the flexible large-area OPV module under different illumination intensities from 55 to 100 mW/cm^2
3. Stability of OPV module
4. The flexible EC thermoregulation device
5. Measurement of real-time temperature by infrared camera
6. Temperature span of flexible EC device and rigid EC device
7. Structure of the OETC system
8. Control unit in OETC system
9. The working mechanism of the OETC system in cooling and warming modes
10. The heat capacity of the heat transfer layer and evaluation of the duration of cooling energy

11. Temperature span of the OETC system at different operation frequencies under the illumination intensity of 100 mW/cm^2

12. The power supplied to EC device by the flexible OPV module is converted to high-voltage DC through VTM under different illumination intensities

13. The temperature span of OETC system at the frequency of 0.75 Hz under 55 mW/cm^2 illumination intensity

14. The outdoor thermoregulation performance of OETC system

15. Comparison of performance between OPV-TE thermoregulation system and OPV-EC thermoregulation system under the illumination intensity of 100 mW/cm^2

16. Average heat flux of the OETC system under different illumination intensities

17. J-V curve of the perovskite photovoltaic module and temperature span of EC device powered by perovskite solar module

18. Power consumption of EC device under different illumination intensities

19. Working mechanism of the OETC system for all-day thermoregulation

20. Self-powered all-day thermoregulatory OETC system

21. Four parallel EC arrays for simultaneous bidirectional thermoregulation

22. Bending measurement of OETC system

23. Thermoregulation of artificial skin with the initial temperature of 34 °C by the OETC under the illumination intensity of 100 mW/cm^2 by solar simulator at varying ambient temperatures

Supplementary Table

1. The performance of the OPV module under different illumination intensities from 55 to 100 mW/cm^2 by solar simulator

Supplementary Movies

1. Bidirectional controllable thermoregulation of four parallel EC arrays
2. Bending measurement of OETC system

Materials and Methods

Preparation of the flexible large-area OPV module

The polymeric donor PBDB-T-F (PM6) (structure shown in **Fig. S1A**) and non-fullerene acceptors (NFAs) material BTP-BO-4Cl (structure shown in **Fig. S1B**) were purchased from Derthon Optoelectronics Materials Science Technology Co LTD. Zinc acetate dihydrate was purchased from Thermo scientific, and chlorobenzene and molybdenum oxide (MoO_3) were purchased from Sigma-Aldrich. Indium tin oxide (ITO)-coated PET substrates were purchased from South China Xiangcheng Technology Co., LTD. Zinc oxide (ZnO) nanoparticles were synthesized following the process of publish work (*54*). New modifying agent (NMA, structure shown in **Fig. S1C**) were synthesized using the method described in previous report (*55*). The flexible large-area OPV module was fabricated by applying an inverted architecture of PET/ITO/ZnO/NMA/active layer/MoO_3/Ag. ITO-coated PET substrate was ultrasonically treated in detergent, deionized water, acetone, and isopropyl alcohol in sequence for 15 min, followed by blowing dry using argon gas. Afterwards, ZnO layer was blade-coated on the pre-cleaned ITO-coated glass at 50 °C in air with a coating velocity of 10 mm/s and a blade–substrate gap of 200 μm, followed by annealing at 120 °C for 15 mins in atmospheric air. After that, a thin film of NMA was blade-coated on ZnO in air with a coating velocity of 10mm/s and a blade–substrate gap of 150 μm. PM6:BTP-BO-4Cl (1:1.2, D: 9 mg/ml) in chlorobenzene with 0.3 vol% 1,8-diiodooctane (DIO) was blade-coated at 60°C with a coating velocity of 20 mm/s and a blade–substrate gap of 400 μm in air. Finally, MoO_3 (~ 6 nm) and Ag (~150 nm) were successively evaporated onto the active layer through a shadow mask (2×10^{-4} Pa). The schematics of the large-area module consisting of seven sub-cells connected in series following the process of publish work (*40*) (**Fig. S1D**). The photograph of the flexible large-area OPV module with 25.2 cm^2 effective area is shown in **Fig. S1E**.

Preparation of the flexible heat transfer layer

The poly (dimethyl siloxane) (PDMS) was purchased from Dow Corning (SYLGARD 184). The boron nitride nanoparticles were purchased from MACKLIN and paraffin phase change microspheres were purchased from Donglin Polymer Materials. PDMS, boron nitride nanoparticles and paraffin phase change microspheres in the weight ratio of 15:2:5 were added into the beaker, and the solution was stirred with a glass rod for 20 min to mix thoroughly. Next,

the mixture was transferred to a mold. Then, the mold was placed in an oven at 100 °C for further curing for 30 min. Finally, flexible heat transfer layer with a thickness of 3 mm was prepared.

Preparation of the flexible EC device

The poly (vinylidene fluoride-trifluoroethylene-chlorofluoroethylene) [P(VDF-TrFE-CFE)] (64.6/26.2/9.2 mol%, Piezotech Arkema group) solution was blade-coated onto a clean glass substrate and the resulting film was heated on hot plat at 120 °C for 2 h to fully evaporate solvent. The single-walled carbon nanotubes (CNT, 5 mg, Nanjing/Jiangsu XFNANO Materials Tech Co., Ltd) was dispersed in a mixture of iso-propyl alcohol (18 mL) and deionized water (2 mL) using tip ultrasonic (1 h). Then, the CNT dispersion was spray-coated on the EC polymer film to form a conductive network. Next, another EC polymer layer was directly fabricated on the CNT network by blade-coating process, and then heated on a hot plat at 120 °C for 2 h to evaporate the solvent. After peeling off the polymer stack from glass substrate, the CNT dispersion was also spray-coated on the rest of the upper and bottom surface of the polymer stack to achieve a complete two-layer EC polymer stack. The overlap of three CNT-based electrodes across the polymer films was defined as active area (2 cm × 4 cm in size) for the EC effect (**Fig. S4**). Finally, as-prepared EC polymer stack was annealed in a vacuum oven at 120 °C for 10 h to increase the degree of crystallinity and improve the polarizability of the polymer. The EC device comprises two laminated sheets with an area of 7 cm × 3 cm and separated by a 3-mm-thick spacer made of PDMS. Each laminate sheet consists of a polyethylene terephthalate (PET) film (50 μm), and a CNT percolation network layer on the surface. We mounted the EC polymer stack on one end of the EC device between the left spacer and the lower laminate sheet, and the other end between the right spacer and the upper laminate sheet. Finally, single-sided polyimide (PI) tapes (30 μm) covered on the outmost CNT-percolation network-coated PET film to electrically insulate the device.

Preparation of the perovskite solar module

ITO substrates were purchased from Advanced Election Technology Co., Ltd. SnO_2 (15%) colloid precursor, N, N-dimethylformamide (DMF) (99.8%), Dimethyl sulfoxide (DMSO) (99.8%) and molybdenum oxide (MoO_3) (99.995%) were purchased from Alfa Aesar. 2,2',7,7'-Tetrakis [N,N-di(4-methoxyphenyl)amino]-9,9'-spiro-bifluorene (Spiro-OMeTAD) was purchased from

Woerjiming (Beijing) technical development institute. Lead Iodide (PbI$_2$) (99.99%), Cesium Iodide (CsI) (99.999%) and 4-tert-butylpyridine (96.0%) were purchased from TCI. Lithium bis(trifluoromethylsulfonyl)-imide (99.9%), Hydroiodic acid aqueous solution (HI) (55-57% w/w), and chlorobenzene (99.9%) were purchased from Sigma-Aldrich. Concentrated hydrochloric acid (HCl) (36-38% w/w), hydrobromic acid (HBr) (AR), methylamine aqueous solution (MA) (40% w/w), and ethyl ether (99.7%) were purchased from Tianjin Bohua chemical reagents Co., Ltd. Formamidine acetate (FAAc) (99%) was purchased from Aladdin. Formamidinium iodide (FAI), methylamine hydrochloride (MACl), and methylammonium bromide (MABr) were synthesized at 0 °C by reacting equal molar ratios of FAAc with HI, MA with HCl, and MA with HBr for 3-4 h, respectively. The solvent was evaporated using rotary evaporation and the solid products were obtained. To improve purity, the products were rinsed with ethyl ether and recrystallized to yield white powders.

The perovskite solar modules were fabricated with an architecture of ITO/SnO$_2$/perovskite/spiro-OMeTAD/MoO$_3$/Ag. The ITO substrates were subjected to ultrasonic treatment in detergent, deionized water, and ethanol, each for 3 cycles, lasting 15 minutes per cycle, sequentially. Before use, the ITO substrates were cleaned with UV-ozone for 20 min. Then, the substrate was spin-coated with the SnO$_2$ precursor (2.5% in H$_2$O) at 3500 rpm for 30 s with a ramp of 3500 rpm s^{-1}, and annealed in ambient air under 170 °C for 30 min. The perovskite films were prepared in a N$_2$-filled glovebox. The perovskite precursor (FA$_{0.90}$Cs$_{0.05}$MA$_{0.05}$Pb(I$_{0.98}$Br$_{0.02}$)$_3$) (1.54 M) was prepared by dissolving PbI$_2$ (1.74 M), FAI (1.38 M), MABr (0.08 M), CsI (0.08 M) and MACl (0.29 M) in mixed solvent (DMF:DMSO = 4:1). Subsequently, the perovskite precursor was spin-coated on the substrate at 4000 rpm for 40 s with a ramp of 4000 rpm s^{-1}. During spin coating, 170 μL anisole was dripped at the end of 20 s. Then, the substrate was put on a hotplate and annealed at 170 °C for 18 min in ambient air. After cooling down to room temperature, the hole transport layer was prepared by spin-coating the Spiro-OMeTAD solution at 6000 rpm for 30 s with a ramp of 6000 rpm s^{-1}. The Spiro-OMeTAD solution was prepared with a concentration of 80 mg mL^{-1} in chlorobenzene, in which 30 μL of tBP and 17.5 μL of Li-TFSI (520 mg mL^{-1} in acetonitrile) were added as additives. Finally, 12 nm of MoO$_3$ and 100 nm silver were deposited by thermal evaporation using a shadow mask to pattern the electrodes. For the scribing process, the ITO substrate was first etched by a laser scriber to form P1 lines. The P2 lines were etched after depositing MoO$_3$ by mechanical scribing. The P3 lines were etched during silver deposition

by a shadow mask. The ITO substrate (5 cm× 5 cm) displayed an active area of 14 cm^2 with 5 sub cells. The J−V curve was measured using a Keithley 2400 source-measurement unit under AM 1.5 G illumination at 100 mW/cm^2 using a SS-F5-3A (Enli tech) solar simulator. The light intensity was calibrated using a certified silicon diode.

Preparation of the artificial skin

The artificial skin was prepared by placing PDMS layer (Dow Corning, 10 cm×10 cm×5 mm) on a resistive heater, and regulated the temperature of the artificial skin by inputting different power. The heat generation of the artificial skin has also been considered by taking the heat generation of human beings as 51 W/m^2 (*46*).

Fabrication of the OETC system

The structural diagram of OETC is shown in **Fig. S7**. The main units of OETC system are OPV module, flexible heat transfer layer, EC device, ESS and voltage control system (VCS). OPV module is connected together with ESS and VCS to provide the voltage for EC device as needed (detailed procedure in **Fig. S8**). The flexible heat transfer layer is sewn onto human clothes, then the OPV module and EC device were fixed to the outside and inside of heat transfer layer by a thermally conductive adhesive (SE-4485, Dow Corning), and cured at 26 °C for 24 h, respectively. With the coordination of all the above mentioned units (**Fig. S9**), OETC allows switching between warming and cooling modes and adjusting them as needed.

Characterization of the OPV module

Current density and voltage (*J–V*) curves were measured in a nitrogen-filled glovebox using a source meter (2400, Keithley Instruments) controlled by a LabVIEW program under standard AM 1.5G (100 mW/cm^2) and a Newport solar simulator (Enli SS-F5-3A, Enli Technology Co., Ltd.). The outdoor sunlight intensity is measured by a solar power meter (SANPOMETER, SM206-SOLAR). The stability of the module was measured under 100 mW/cm^2 illumination by solar simulator in the nitrogen-filled glove box at temperature of 25 °C.

Comparison of the EC device driven by OPV module and electric supply

The high voltage for EC device provided by electric supply is using a high-voltage power source (Dongwen, DW-P103-0), while the high voltage provided by OPV module is using a voltage transformation module (VTM, Dongwen) as shown in **Fig. 2D**.

Calculation of the average heat flux and power consumption

The heat flux ($\Phi_{\text{heat flux}}$) of the OETC system is measured by heat flux sensor (Omega HFS-5). The details of the average heat flux of the OETC system under different illumination intensities can be found in **Fig. S16**. The $W_{Power\ consumption}$ is the total electric energy consumption of OETC system in one operation period. The calculate $W_{Power\ consumption} = \int_{t_1}^{t_2} V_{EC} \times I_{EC} dt$ (**Fig. S18**), where t_1 and t_2 are the start and the end time of an entire operation period, and V_{EC} and I_{EC} are the measured voltage (**Fig. S12**) and current (**Fig. S18A**) using an oscilloscope (RIGOLDS1104Z Plus), respectively.

Supplementary Text

Calculation of the required OPV module area to provide all-day thermoregulation for individual space travel

During individual space travel, the theoretical area of spacesuit ($S_{spacesuit}$) is around 1.85 m^2. According to **Fig. S20**, an OPV module with an active area ($S_{OPV-\text{all day thermoregulation}}$) of 25.2 cm^2 have sufficient power to drive EC device with the active area ($S_{EC-\text{all day thermoregulation}}$) of 8 cm^2 to achieve all-day thermoregulation. To realize individual space travel all-day thermoregulation, the as-prepared effective area of OPV module is

$$S_{as-prepared\ OPV\ unit\ area} = \frac{S_{OPV-\text{all day thermoregulation}}}{S_{EC-\text{all day thermoregulation}}} \times S_{spacesuit} \tag{S1}$$

In space, the solar flux in one astronomical unit (I_{space}) is 136.7 mW/cm^2, if assuming a 45% PCE solar cell device is to be used, the luminous energy ratio (η) of the solar cell device with PCE of 45% in space to solar cell device with PCE of 11.85% on surface earth is

$$\eta = \frac{I_{space} \times 45\%}{I_{surface\ earth} \times 11.85\%} \tag{S2}$$

With the continuingly improved solar cell performance including that of flexible OPV, the required OPV unit area

$$S_{required\ OPV\ unit\ area} = \frac{S_{as-prepared\ OPV\ unit\ area}}{\eta} \tag{S3}$$

Based on $Eq.(S1)$, the calculated $S_{as-prepared\ OPV\ unit\ area}$ is 5.83 m^2 ($\frac{25.2\ cm^2}{8\ cm^2} \times 1.85\ m^2$)

Based on $Eq.(S2)$, the calculated η is 5.19 ($\frac{136.7\ mW/cm^2 \times 45\%}{100\ mW/cm^2 \times 11.85\%}$)

Based on $Eq.(S3)$, the calculated $S_{required\ OPV\ unit\ area}$ is 1.12 m^2 ($\frac{5.83\ m^2}{5.19}$)

Definition of Cu-PE, TiO$_2$/PLA/PTFE, NFM, Janus film and NanoPE in Fig. 3F

"Cu-PE" is defined as the bilayer structure by depositing copper-Cu onto the PE film (1). "TiO$_2$/PLA/PTFE" is defined as the multilayer metafabric consists of TiO$_2$-PLA composite woven textile laminated with a PTFE layer (4). "NFM" is defined as the nanofiber membrane (NFM) comprises polyamide 6 (PA6) nanofibers and SiO$_2$ submicron spheres (5). "Janus film" is defined as the Janus film consists of cooling side (SiO$_2$@PDMS/Al layer) and warming side (CNTs@PDMS layer) (45). "NanoPE" is defined as the dual-mode textile is composed of nanoporous polyethylene (nanoPE) layer (46).

Supplementary Figure

1. Preparation of the flexible large-area OPV module
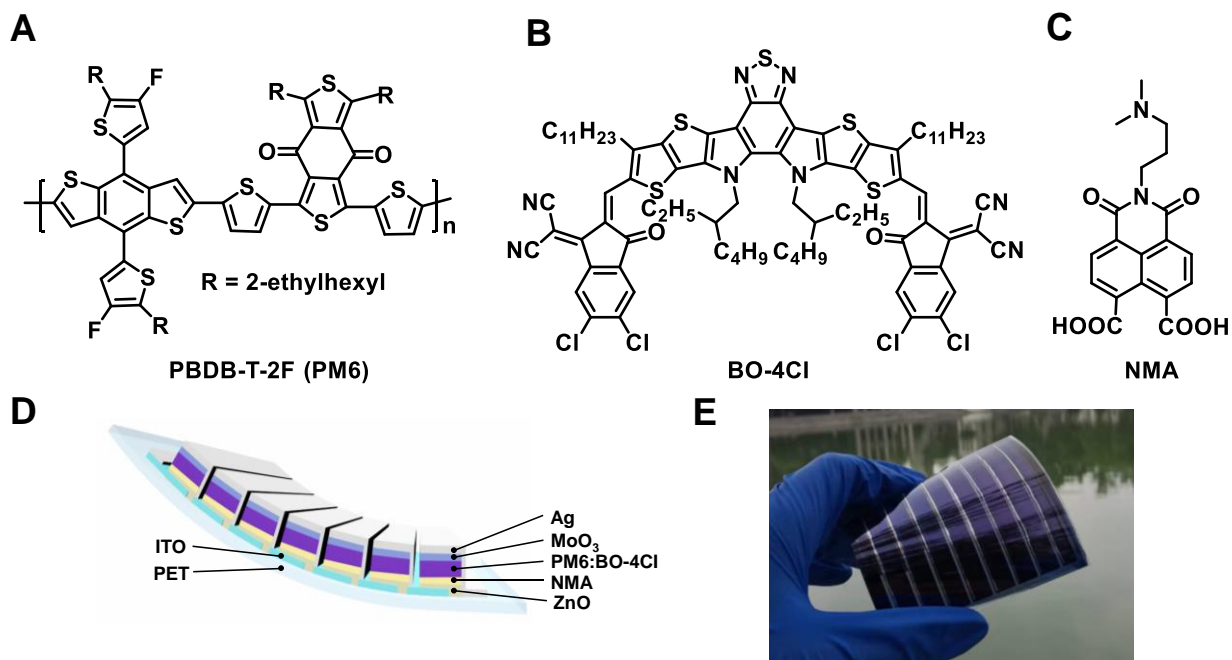
Fig. S1. Flexible large-area OPV module. Molecular structures of polymer donors PM6 (PBDB-T-F) (**A**), NFAs material BTP-BO-4CI (**B**) and NMA (**C**) used in this study. Structure diagram (**D**) and photograph (**E**) of the flexible large-area OPV modules.

Fig. S1A, B & C show molecular structures of the polymer donors PM6 (PBDB-T-F), NFA materials BTP-BO-4CI and the new modifying agent (NMA) used in this study, respectively. **Fig. S1D** shows the schematic of the large-area OPV module consisting of seven sub-cells by applying an inverted architecture of ITO/ZnO/NMA/ PM6:BTP-BO-4CI /MoO$_3$/Ag. **Fig. S1E** is photograph of the flexible OPV module with the effective area of 25.2 cm^2.

2. ***J-V* curve of the flexible large-area OPV module under different illumination intensities from 55 to 100 mW/cm^2**
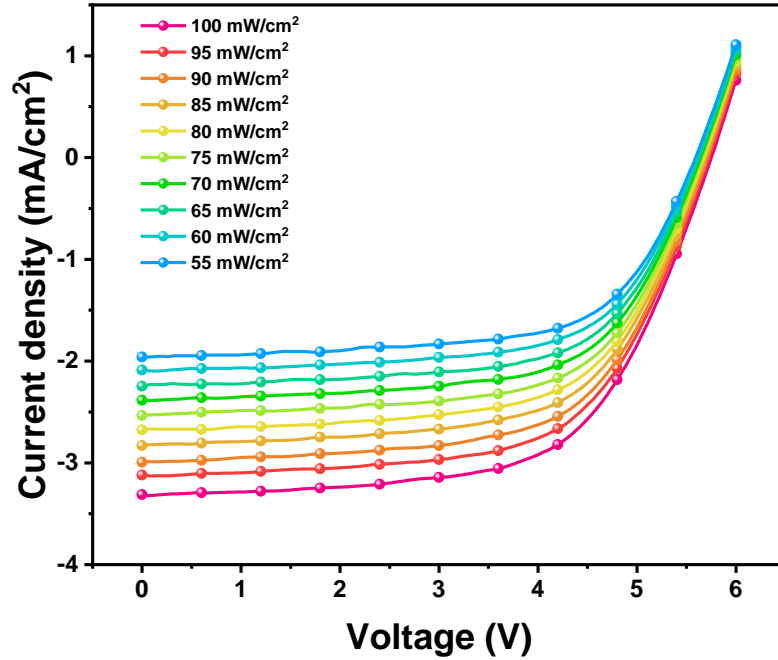

Fig. S2. *J-V* curve of the flexible OPV module under different illumination intensities from 55 to 100 mW/cm^2.

Fig. S2 shows the current density and voltage (*J-V*) of the flexible OPV module as a function of different illumination intensities from 55 to 100 mW/cm^2 using a solar simulator. The *J-V* curves were obtained by a Keithley 2400 source-measure unit. The maximum voltage of 5.75 V and current density of 3.31 mA/cm^2 were obtained at the illumination intensity of 100 mW/cm^2.

3. Stability of OPV module
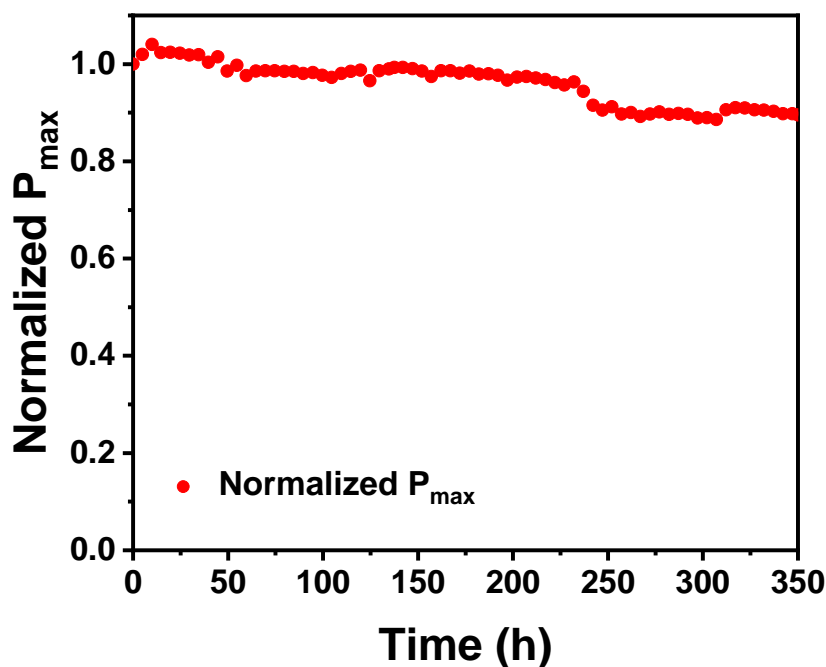
Fig. S3. Stability of OPV module. The stability measurement of the OPV module under the illumination of 100 mW/cm^2 by solar simulator.

As shown in **Fig. S3**, the stability of OPV module was measured under the illumination of 100 mW/cm^2 by solar simulator in nitrogen-filled glove box at temperature of 25 °C. The module showed good photostability and its initial efficiency of 89.5 % can be maintained even after 350 h continuous illumination.

The flexible and large size OPV module used in this study was directly fabricated in our own lab (*40*), which has been designed and fabricated for the easy and convenient integration with the EC unit as shown in the **Fig. S3**. This OPV module could be estimated to last approximately 3000 h, but its lifetime is lower than the best modules reported in the literature (T80 (the time required to reach 80% of initial performance) for 7572 h and extrapolation of > 56000 h) (*55, 56*). However, by either improving our lab-prepared OPV module or using an external better OPV module if available, the lifetime of our OETC system could be significantly improved.

4. The flexible EC thermoregulation device

Fig. S4. The photograph of the flexible EC thermoregulation device.

Fig. S4 shows the flexible EC device (7 cm by 3 cm by 0.3 cm) comprises two transparent flexible sheets made of conductive CNT coated on a 50 μm thick PET film that serves as the laminate sheets for electrostatic actuation. The S-shaped EC polymer stack is fixed onto a PDMS frame spacer (3-mm-thick). Due to its excellent flexibility, it can achieve good thermal contact with surface of human skin, so as to realize efficient thermoregulation of human body. By regulating the input voltage signal, the flexible EC thermoregulation device can realize continuous heat transfer between the skin and the heat transfer layer.

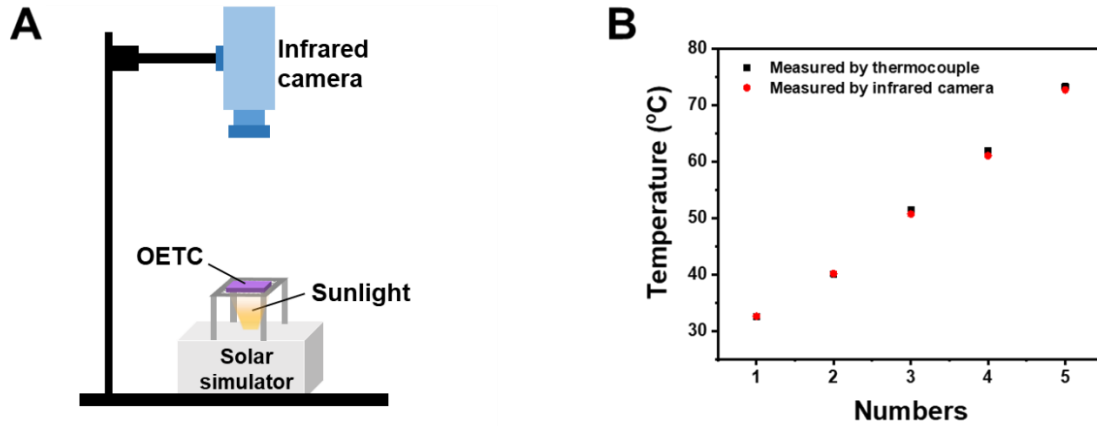## 5. Measurement of real-time temperature by infrared camera

Fig. S5. Measurement of real-time temperature by infrared camera. (**A**) Schematic illustration of measuring system for thermoregulatory performance of OETC system. (**B**) Temperature comparison of EC device tested by infrared camera and thermocouple.

To collect real-time temperature data, we used infrared camera (Fotric 618C-L29) to record the surface temperature of OETC system, as shown in **Fig. S5A**. We have followed the published and well accepted prototype (*36, 37*) to make the calibration. We first put the K-type thermocouple in boiling water and ice-water mixture to calibrate thermocouple test results. The emissivity of each object was calibrated using a thermocouple with precise temperature as shown in **Fig. S5B**.

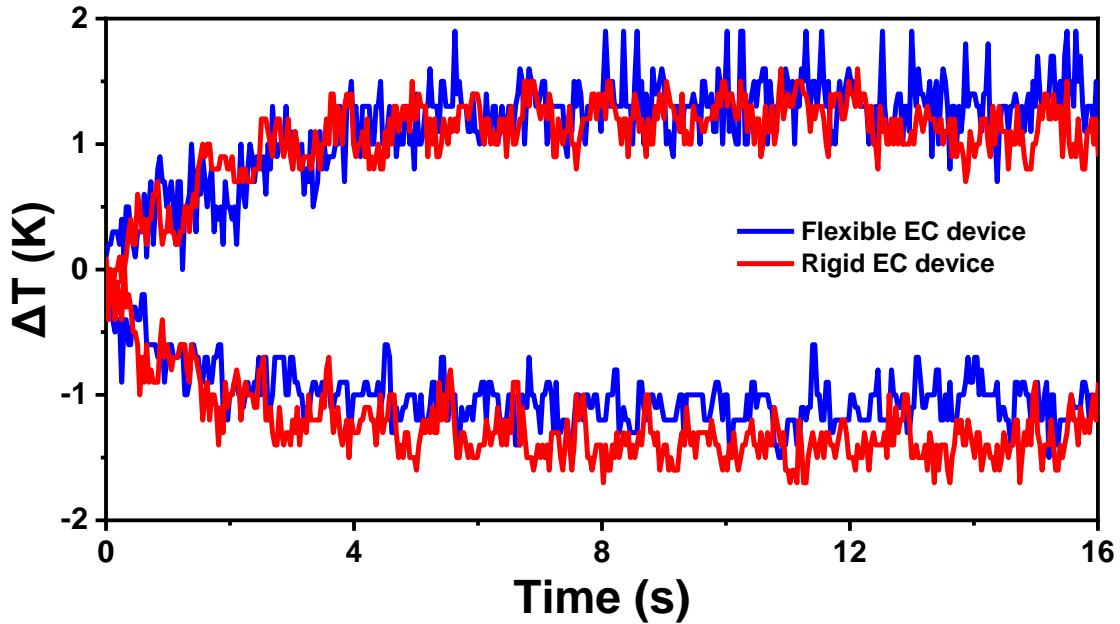**6. Temperature span of flexible EC device and rigid EC device**

Fig. S6. Temperature span of flexible and rigid EC devices powered by the flexible OPV module under the illumination intensity of 70 mW/cm^2 using solar simulator.

In **Fig. S6**, the temperature span of flexible and rigid EC devices was measured under the illumination intensity of 70 mW/cm^2 by solar simulator (Enli SS-F5-3A, Enli Technology Co., Ltd.). The flexible EC device guarantees almost the same thermoregulatory performance as the rigid EC device, while satisfying the flexible needs of wearable thermoregulatory.
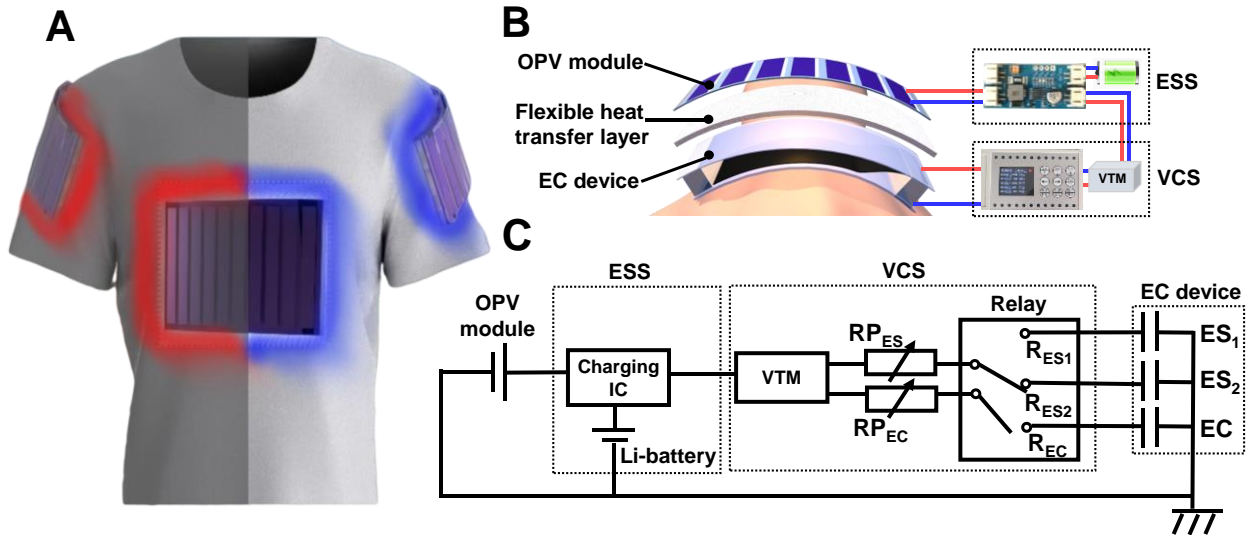
7. Structure of the OETC system

Fig. S7. Structure of the OETC system. (**A**) The schematic of the OETC. (**B**) The main units of OETC system with OPV module, flexible heat transfer layer, EC device, ESS and VCS. (**C**) The working circuitry of the OETC system.

The schematic of the OETC is shown in **Fig. S7A**. The OPV module is connected together with the energy storage system (ESS, including charging IC and Li-battery) and voltage control system (VCS, including VTM, resistance potentiometer and relay) to provide the voltage for EC device as needed (**Fig. S7B & C**).

Under practical application conditions, the entire OETC system can be completely encapsulated by PI or other film (could also be waterproof), which could provide good insulation to avoid direct contact between the device and skin, reducing the high voltage safety concerns influence of the sweats from human body.

During the operating state, the OPV produces a power only at the level of (Pmax of 298.58 mW with Voc of 5.75 V and Isc of 83.4 mA). So, at the state of operation, with an operating voltage of 2000 V, the neat current is only nearly 0.1 mA, which is far below the safe current for human beings (50 mA) as specified in a working guide (*57*).

Even if there is leakage, the current generated in actual contact with the human body is limited, we thought this might be also rather safe, as that like the static electricity generated by the friction of clothes (~2500 V) (*58*) and the voltage generated by the piezoelectric ceramics in lighters (~2000 V) (*59*), which will not cause any damage to human health.

The flexible heat transfer layer is sewn onto human clothes, and the OPV module and EC device were fixed to the outside and inside of heat transfer layer, respectively. With the coordination of all the above mentioned units, OETC allows switching between warming and cooling modes and adjusting them as needed.
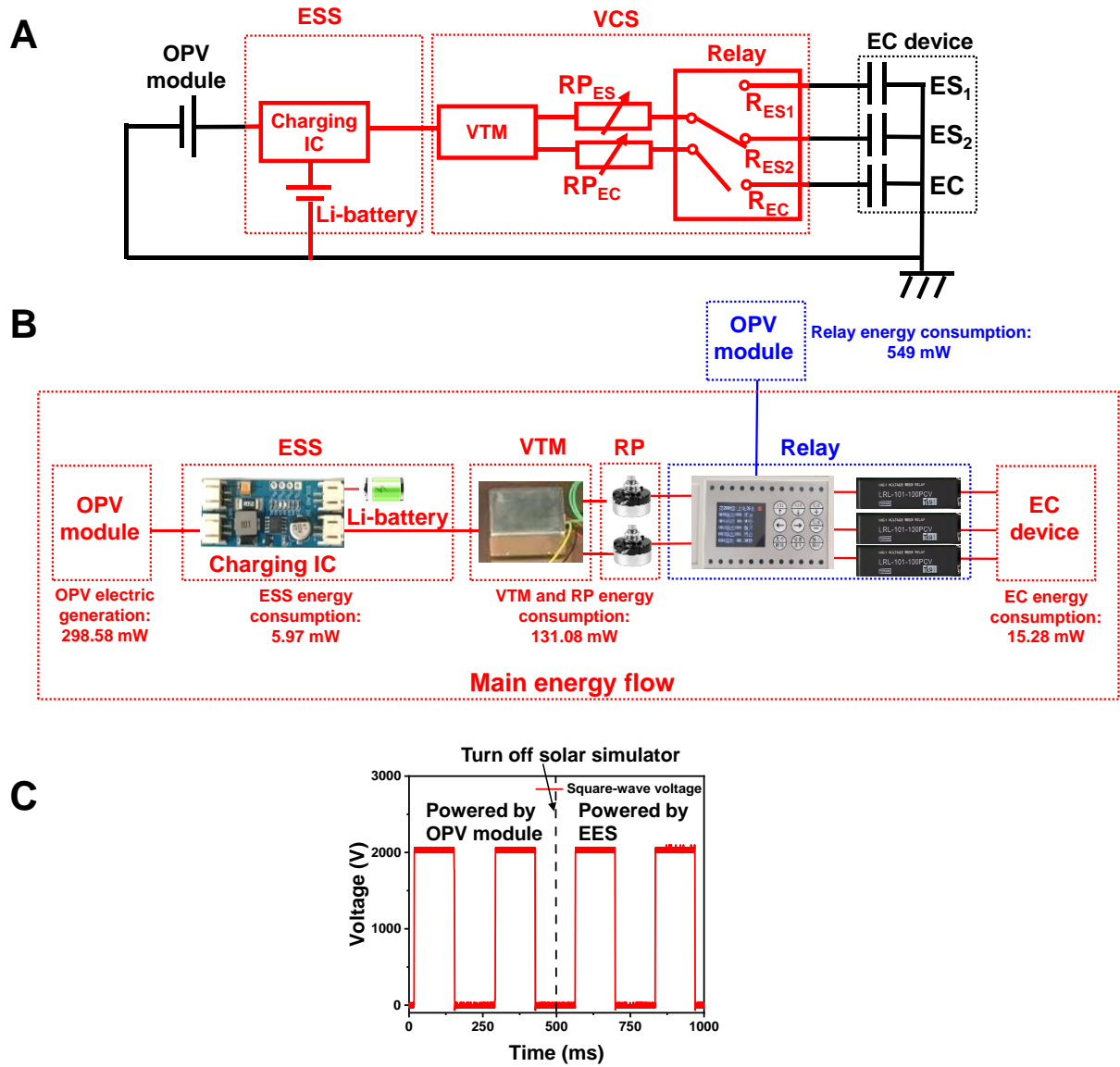
8. Control unit in OETC system

A

B

C

Fig. S8. Control unit in OETC system. The circuitry (**A**) and photographs (**B**) of each component in OETC system. (**C**) The comparison of voltage provided by OPV module and ESS applied to EC device.

As shown in **Fig. S8A & B**, charging integrated circuit chip (Charging IC, 4.6 g, CN3791 MPPT Solar Charger 6 V, WenDaoGuangFu) is connected to OPV module, Li-battery (42.5 g, CG Li-ion 18650 3.7 V 1500 mAh, WenDaoGuangFu) and voltage transformation module (VTM, 74.7 g, 5 V to 2000 V, Dongwen). VTM can convert the low voltage of OPV module into high voltage

19

to provide the voltage for EC effect and electrostatic force of EC device. Moreover, the voltage can be adjusted by the resistance potentiometer (RP$_{ES}$ and RP$_{EC}$, 4.2 g). And the relay (384.4 g, LRL-102-100PCV, Toward) can form the different frequencies and phase of the square-wave voltage.

The whole weight of ESS (Charging IC, Li-battery) is 46.5 g, and the whole weight of VCS (VTM, RP, Relay) is 463.3 g. However, OPV and EC have weight of only 2.29 g and 4.31 g, respectively. In addition, the power consumption of EC device, ESS and VTM and RP, and Relay is 15.28, 5.97, 131.08 mW and 549 mW, respectively. In the calculation of power consumption in the main manuscript, we did not include the energy cost from relay in our OETC main energy flow, and the reason is: the relay is only used to control the voltage waveform and phase, which is not consumed energy from the main energy flow paths (OPV module to EC device). In this study, one relay powered by another OPV module can be used to control 4 units, and we believe that the relay could control more units to reduce the overall power consumption. If the energy consumption of the relay is not included, the efficiency of our entire OETC system will be very high. Even if we consider the energy consumption of the relay, the total system is still self-powered only by sunlight. It is worthwhile to note that, the extra weight mainly comes from ESS and VCS, while the extra power consumption mainly comes from the Relay. They were used commercial components and should be optimized in future and can also be used to control multiple units, thus reducing the overall weight and power consumption.

Furthermore, all the power consumption of the entire system is from OPV module. And the OPV module can provide sufficient energy to power the entire system, so the OETC system is self-sustainable.

We have been working with our suppliers to design new integrated devices, and we expect that the power consumption of this part can be greatly reduced.

Moreover, OETC can store additional energy in the Li-battery during the daytime and release the stored energy at night to continue driving the EC thermal management system. **Fig. S8C** compared the voltage provided by OPV module and ESS applied to EC device. It indicates that the voltage provided by ESS is the same as that provided by OPV module which guarantees all-day thermoregulation.

9. The working mechanism of the OETC system in cooling and warming modes
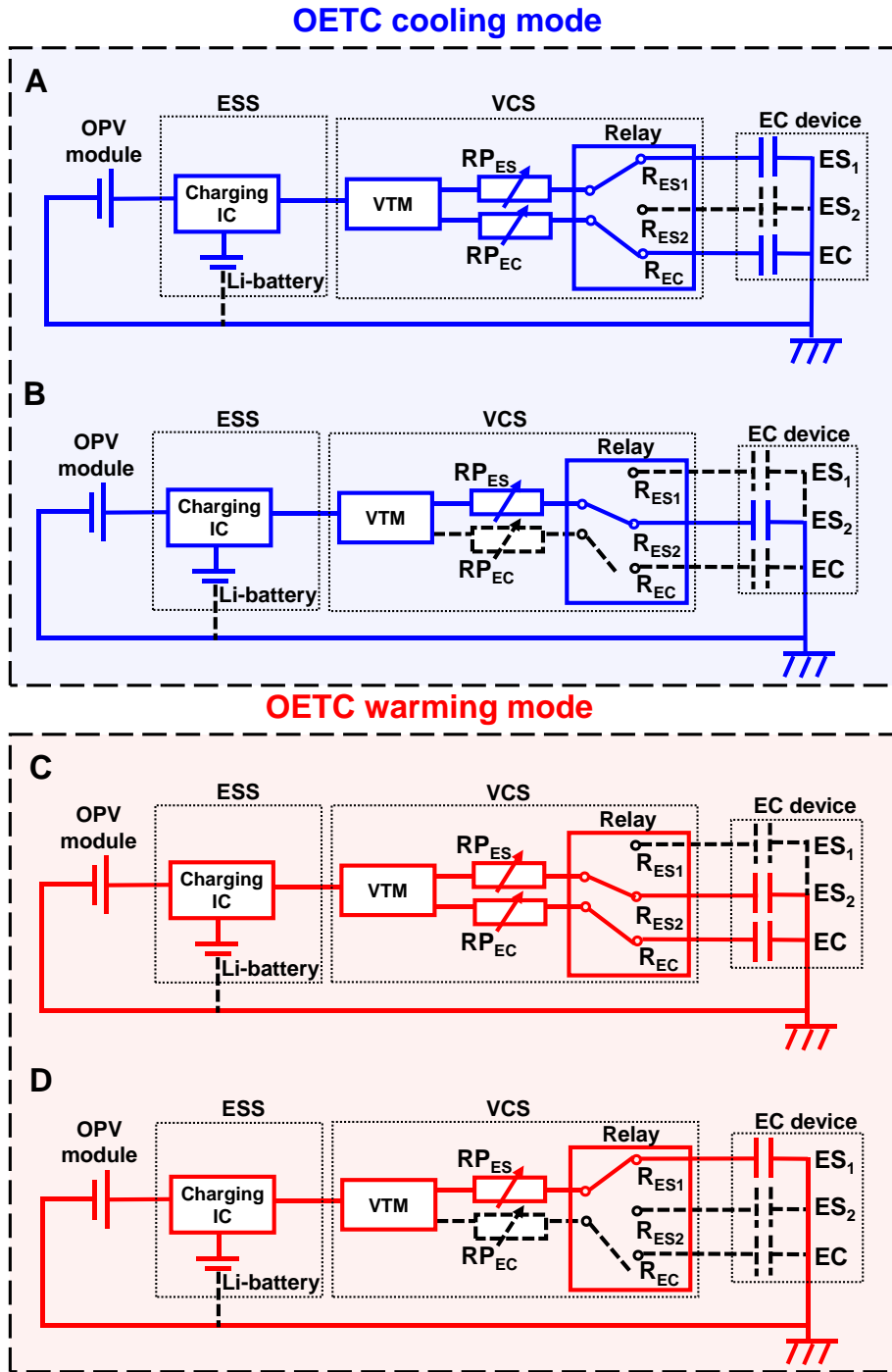

Fig. S9. Working mechanism of the OETC system in cooling (A & B) and warming (C & D) modes.

During the operation, the cooling mode includes the following steps: (i) By switching the electric relay R_{ES1} on, an electrostatic field is applied between the top CNT-based electrode of EC device and the outer CNT electrode of the EC polymer stack. EC polymer stack moves toward the top flexible heat transfer layer (as a heat sink) by electrostatic force; (ii) By switching the electric relay R_{EC} on, the EC polymer stack is heated up by applying an electric field on the EC polymer stack and thus heat transfer from the EC polymer stack to the flexible heat transfer layer (**Fig. S9A**); (iii) When the relay is switched from R_{ES1} to R_{ES2}, the EC polymer stack moves toward the bottom human skin (as a heat source) by the electrostatic force; (iv) By switching the electric relay R_{EC} off, the EC polymer stack is cooled down by removing the electric field and thus heat transfer from the human skin to the EC polymer stack to realize one cycle of skin cooling (**Fig. S9B**).

For the warming mode, it is achieved by changing the heat transfer to the opposite direction, simply by changing sequence of the four steps described above, which is reached by simply adjusting the phase of square wave voltage. Correspondingly, the warming mode has similar steps to the cooling mode, but with opposite heat transfer effect: (i) By switching the electric relay R_{ES2} on, the EC polymer stack moves toward the bottom human skin which needs to be warmed up by the electrostatic force; (ii) By switching the electric relay R_{EC} on, the EC polymer stack is heated up by applying an electric field on the EC polymer stack and thus heat transfer from the EC polymer stack to the human skin (as a heat sink) (**Fig. S9C**); (iii) When the relay is switched from R_{ES2} to R_{ES1}, the EC polymer stack moves toward the top flexible heat transfer layer (as a heat source) by electrostatic force; (iv) By switching the electric relay R_{EC} off, the EC polymer stack is cooled down by removing the electric field and thus heat transfer from the flexible heat transfer layer to the EC polymer stack to finish one cycle of skin warming (**Fig. S9D**). Therefore, the bidirectional controllable thermoregulation for cooling and warming is easily implemented.

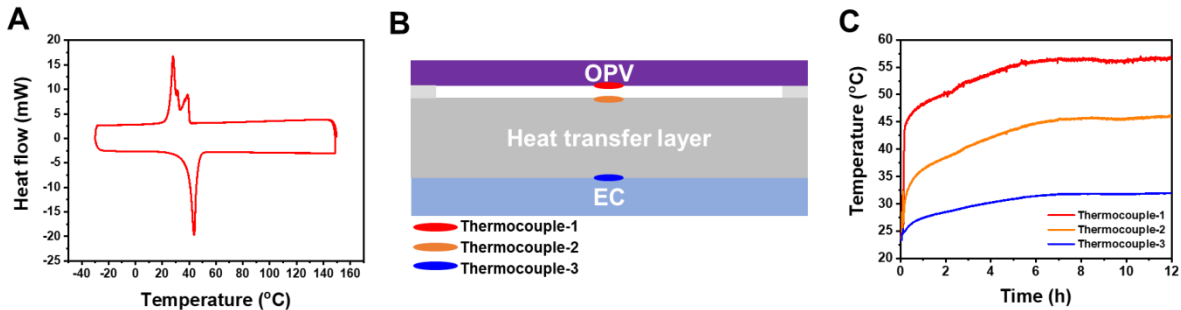**10. The heat capacity of the heat transfer layer and evaluation of the duration of cooling energy**

Fig. S10. Performance of the heat transfer layer. (**A**) The characterization of the heat transfer layer by differential scanning calorimetry. (**B**) Schematic illustration of the setup for measuring the temperature change under sunlight expose. (**C**) The temperature change of OETC system under the standard AM 1.5G (100 mW/cm^2) by solar simulator.

In fact, the heat transfer layer plays an important role as a heat sink during the cooling mode, especially under sunlight, so we added paraffin phase change capsules to the heat transfer layer, which greatly improves the heat storage capacity of the heat transfer layer. In order to measure the actual heat capacity of the heat transfer layer, we performed DSC measurement of the heat transfer layer (**Fig. S10A**). During the phase change (20-45 °C), the heat capacity of heat transfer layer (29.47 g) is 157.65 J/g, which can absorb 4645.95 J of heat. Since the heat flux of the device in cooling mode is barely 28.76 mW/cm^2, which enables our OETC system to maintain good thermal management performance for 5.61 h, without consideration of heat dissipation from heat transfer layer to the air. During actual operation, the heat transfer layer could effectively exchange heat with the surrounding environment, which can enable the OETC system to maintain good thermal management performance for a longer period of time.

To further evaluate the duration of its cooling energy under sunlight, we measured the temperature change of OETC system under the standard AM 1.5G (100 mW/cm^2) by solar simulator. The schematic illustration of the setup for measuring the temperature change under sunlight expose is shown in **Fig. S10B**. As shown in **Fig. S10C**, the temperature of OPV and EC units reach at 55 and 32 °C, respectively, under a 12 h sunlight expose. As indicated in **Fig. S10C**, the temperature change of EC device is very small (from the initial 25 °C to the equilibrium 32 °C),

which is much lower than upside temperature of heat transfer layer (45 °C). Since the flexible heat transfer layer contains a phase change material that absorbs the heat from the sunlight, the heat transfer layer can effectively absorb and block the heat transfer from sunlight to EC device.

11. Temperature span of the OETC system at different operation frequencies under the illumination intensity of 100 mW/cm^2
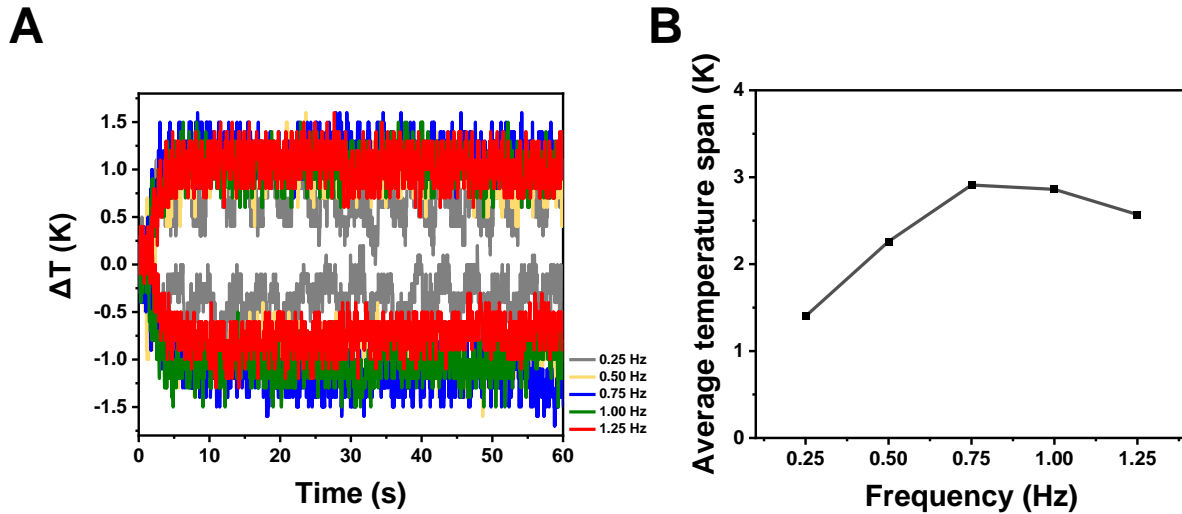
Fig. S11. Temperature span of the OETC system at different operation frequencies under the illumination intensity of 100 mW/cm^2 by solar simulator.

Fig. S11 compares the temperature span of the OETC system at different operating frequencies using a solar simulator at a light intensity of 100 mW/cm^2. Although the OETC system can operate at higher frequencies, the frequency of the OETC system that gives maximum temperature span of 2.9 K is 0.75 Hz due in part to the time need to transfer the heat from the EC stack to the human skin and flexible heat transfer layer.

12. The power supplied to EC device by the flexible OPV module is converted to high-voltage DC through VTM under different illumination intensities
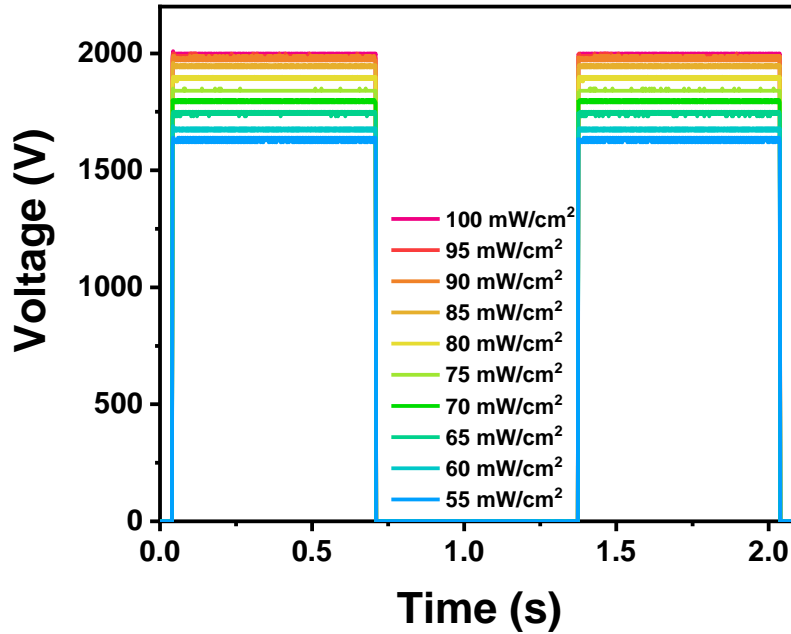

Fig. S12. The power supplied to EC device by the flexible OPV module is converted to high-voltage DC through VTM at different illumination intensities from 55 to 100 mW/cm^2.

As shown in **Fig. S12**, the power supplied to EC device by the flexible OPV module is converted to high-voltage DC through VTM at different illumination intensities from 55 to 100 mW/cm^2. We use an oscilloscope to monitor the power supplied by OPV module to the EC device. The frequency of square-wave voltage is at 0.75 Hz under different illumination intensities. With the increase of illumination intensity, the flexible OPV module can reach higher voltages, and thus the input voltage of the EC device (V_{EC}) increases, which results in a higher thermoregulatory performance of the OETC.

13. The temperature span of OETC system at the frequency of 0.75 Hz under 55 mW/cm^2 illumination intensity
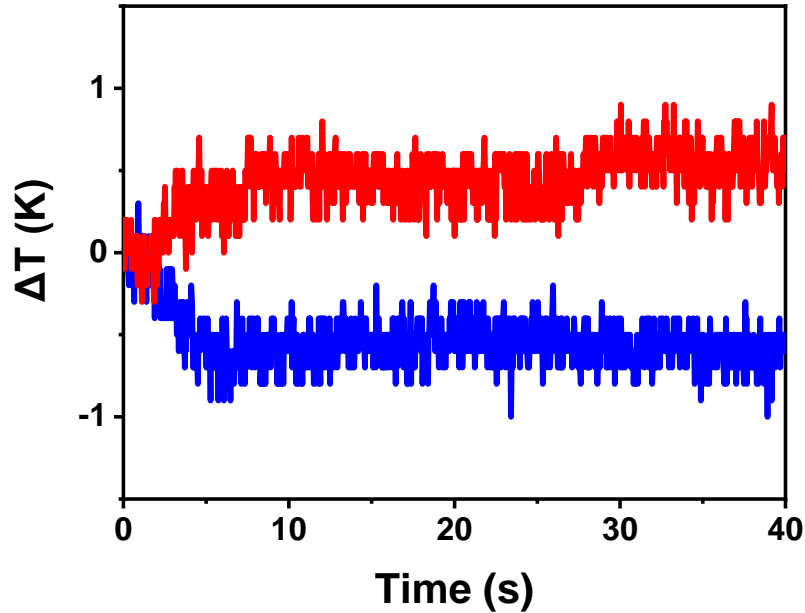

Fig. S13. The temperature span of the OETC system at the frequency of 0.75 Hz under 55 mW/cm^2 illumination intensity by solar simulator.

We also measured the performance of the OETC system at lower illumination intensity of 55 mW/cm^2 at 0.75 Hz. As shown in **Fig. S13**, the OETC system still has good bidirectional thermoregulation performance at low illumination intensity of 55 mW/cm^2, with the bidirectional thermoregulatory temperature span of 1.1 K at 0.75 Hz.

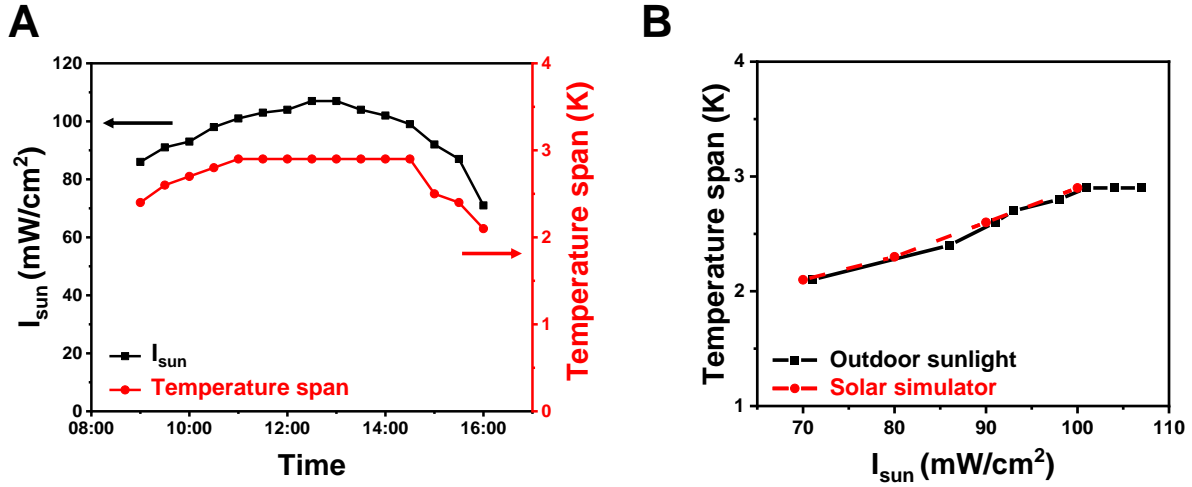**14. The outdoor thermoregulation performance of OETC system**

Fig. S14. The outdoor thermoregulation performance of OETC system. (**A**) The outdoor thermoregulation performance of the OETC system. (**B**) Comparison of temperature span of OETC system under outdoor sunlight and solar simulator.

We also demonstrated the outdoor thermoregulation performance of our OETC system by direct solar radiation under clear sky conditions from 9:00 to 16:00 in Tianjin, China (38°59′ 65″ N, 117°21′ 16″ E, August 3, 2022) (**Fig. S14A**). The sunlight intensity is measured by a solar power meter (SANPOMETER, SM206-SOLAR). Although the intensity of outdoor sunlight fluctuates a lot with time, our OETC system still shows good thermoregulatory ability at different light intensities. In **Fig. S14B**, when the outdoor sunlight intensity is the same as the simulated light intensity, the OETC system exhibits almost the same thermoregulation (**Fig. 2C & Fig. S14B**). The whole process does not need to involve other external energy sources, realizing self-powered cooling with zero-energy consumption.

15. Comparison of performance between OPV-TE thermoregulation system and OPV-EC thermoregulation system (OETC) under the illumination intensity of 100 mW/cm^2
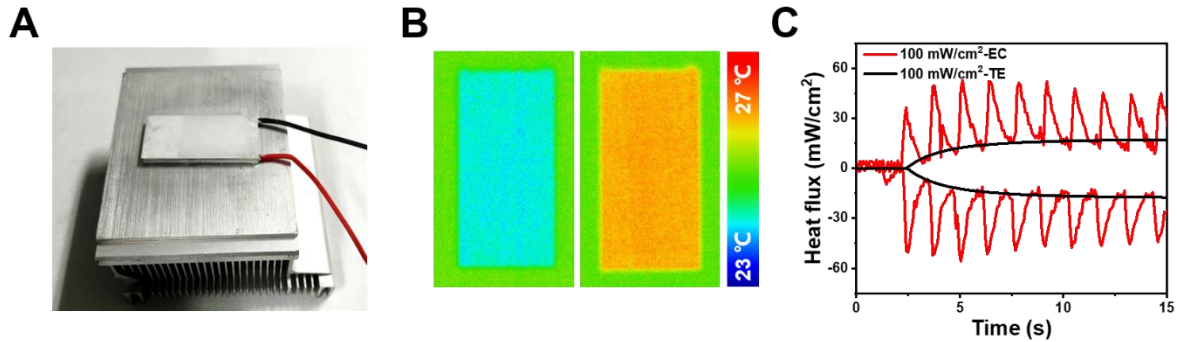

Fig. S15. Comparison of the performance between OPV-TE thermoregulation system and OPV-EC thermoregulation system under the illumination intensity of 100 mW/cm^2 by solar simulator. (**A**) photograph of a commercial TE device (2 cm × 4 cm in size) on an aluminum heat sink. (**B**) Infrared thermal images of the cooling and warming modes of OPV-TE system under the illumination intensity of 100 mW/cm^2. (**C**) Comparison of heat flux of OPV-TE and OPV-EC thermoregulation systems under the illumination intensity of 100 mW/cm^2.

We used the same OPV module (V_{oc} of 5.75 V, J_{sc} of 3.31 mA/cm^2, and P_{max} of 298.58 mW) to directly drive commercial TE thermoregulation device (2 cm × 4 cm in size), as shown in **Fig. S15**. The temperature span (**Fig. 2E**) and heat flux (**Fig. S15C**) of EC and TE devices were measured by infrared camera and heat flux sensor, respectively. Its effective area is equivalent to that of an EC thermoregulation device under the illumination intensity of 100 mW/cm^2 to compare their thermoregulation performance (**Fig. S15A**). **Fig. S15B** shows the infrared thermal images of the cooling and warming modes of OPV-TE system under the illumination intensity of 100 mW/cm^2 by solar simulator. In addition, the average heat flux (**Fig. S15C**) of OPV-EC system is 28.76 mW/cm^2, while the OPV-TE system shows the average heat flux is only 16.79 mW/cm^2 under the same illumination intensity of 100 mW/cm^2.

16. Average heat flux of the OETC system under different illumination intensities
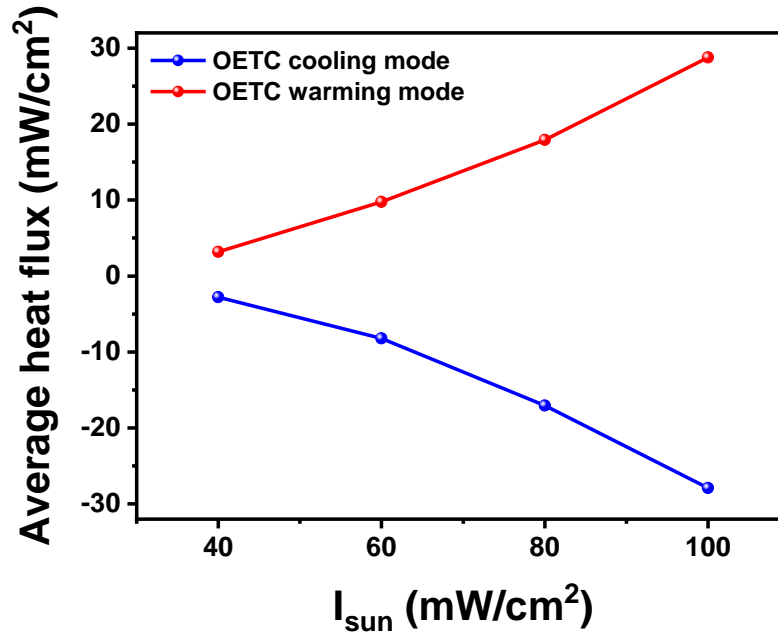

Fig. S16. Average heat flux of the OETC system measured by heat flux sensor under different illumination intensities from 40 to 100 mW/cm² by solar simulator.

Fig. S16 shows average heat flux of the OETC system measured by heat flux sensor under different illumination intensities from 40 to 100 mW/cm² by solar simulator at 0.75 Hz. The maximum average heat flux of the OETC is 27.89 mW/cm² of cooling mode and 28.76 mW/cm² of warming mode under 100 mW/cm² illumination intensity at 0.75 Hz. Even at a relatively low illumination intensity of 40 mW/cm², the average heat flux of the OETC can reach 2.79 mW/cm² of cooling mode and 3.17 mW/cm² of warming mode.

17. J-V curve of the perovskite photovoltaic module and temperature span of EC device powered by perovskite solar module
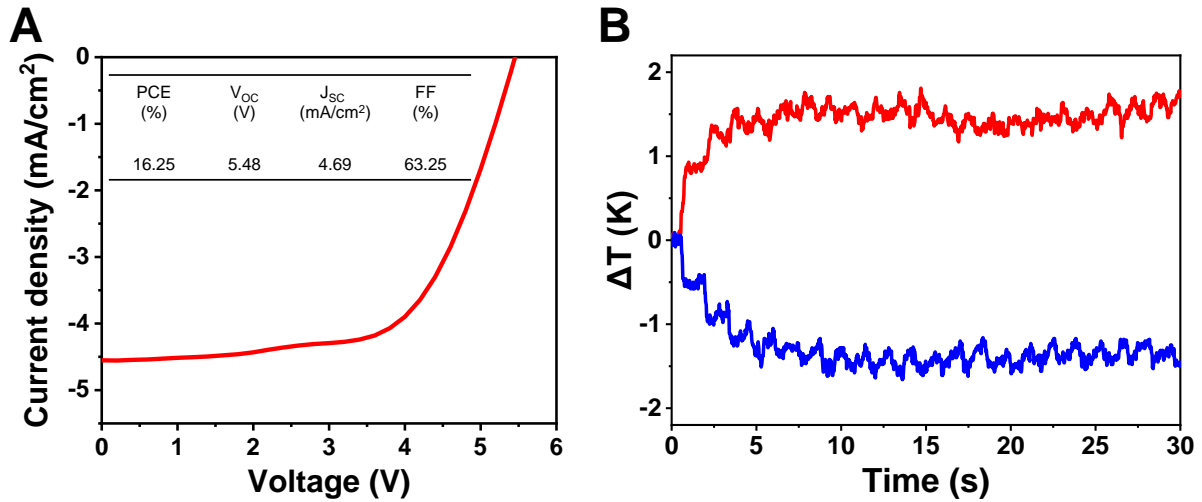

Fig. S17. J-V curve of the perovskite photovoltaic module and temperature span of EC device powered by perovskite solar module. (A) *J-V* curve of the perovskite solar module under the illumination intensity of 100 mW/cm^2. **(B)** Temperature span of the EC device powered by the perovskite solar module under the illumination intensity of 100 mW/cm^2 at 0.75 Hz.

Fig. S17A shows the J-V curve of the perovskite solar module measured at reverse scan under simulated one-sun AM 1.5G illumination (100 mW/cm^2). The device with active area of 14 cm^2 shows a V_{OC} of 5.48 V, a J_{SC} of 4.69 mA/cm^2, and a fill factor (FF) of 63.25%, yielding a PCE of 16.25%. The corresponding P_{max} is 227.5 mW. Compared with the thermal management performance of EC device powered by OPV module in **Fig. 2C**, the EC device powered by the perovskite solar module (**Fig. S17B**) indicates almost same results.

18. Power consumption of EC device under different illumination intensities
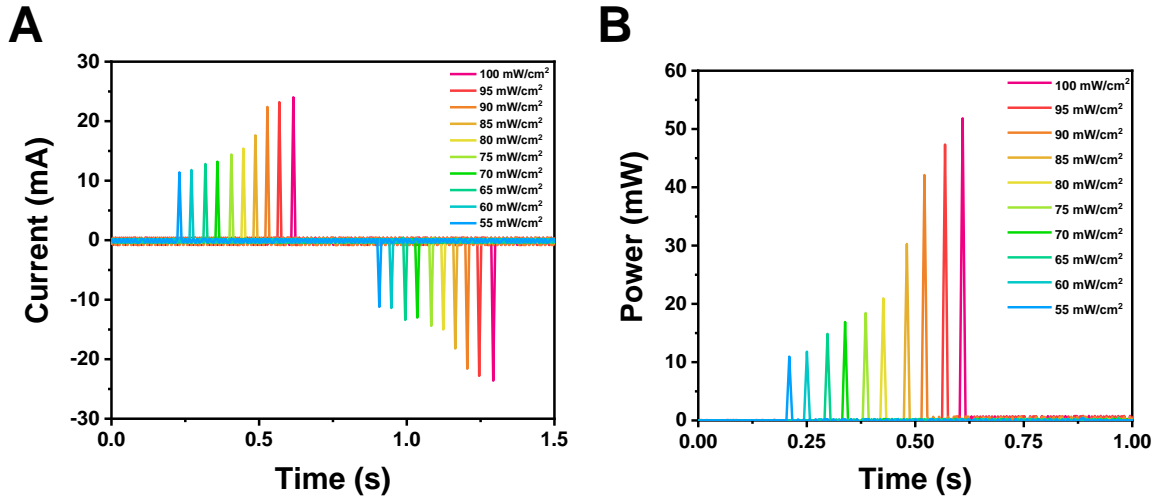

Fig. S18. Power consumption of EC device (W$_{Power\ consumption}$) at the frequency of 0.75 Hz under different illumination intensities from 55 to 100 mW/cm^2 by solar simulator. (**A**) Current of EC device (I$_{EC}$). (**B**)Power consumption of EC device.

We measured the power consumption of EC device under different illumination intensities from 55 to 100 mW/cm^2 by solar simulator in **Fig. S18**. The largest average power consumption of the EC device is only 1.91 mW/cm^2 at 0.75 Hz under the illumination intensity of 100 mW/cm^2 due to its low energy consumption. The calculated $W_{Power\ consumption} = \int_{t_1}^{t_2} V_{EC} \times I_{EC} dt$ (**Fig. S18B**), where t$_1$ and t$_2$ are the start and the end time of an entire operation period, and V$_{EC}$ and I$_{EC}$ are the measured voltage (**Fig. S11**) and current (**Fig. S18A**) using an oscilloscope (RIGOLDS1104Z Plus), respectively.

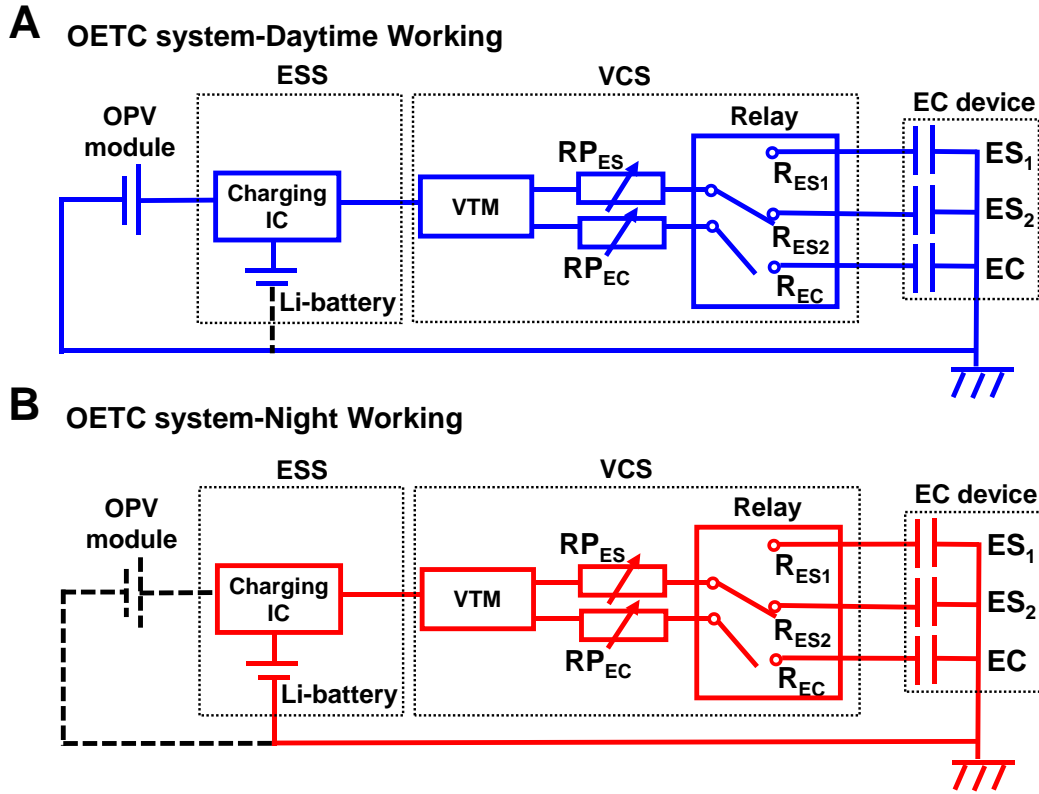## 19. Working mechanism of the OETC system for all-day thermoregulation

Fig. S19. Working mechanism of the OETC system for all-day thermoregulation. (**A**) OETC system daytime working mechanism. OPV module can provide continuous energy supply to the EC devices during the daytime. (**B**) OETC system night working mechanism. The surplus energy collected and stored in ESS during the daytime is automatically switched to power the entire system at night with no extra energy input.

Fig. S19 shows the working mechanism of the OETC system for all-day thermoregulation. OPV module can provide continuous energy supply to the EC device during the daytime (**Fig. S19A**). Considering that the PCE of our OPV module (with an active area of 25.2 cm^2) is 11.85% under standard AM 1.5G (100 mW/cm^2) and the energy consumption of EC device (with an active area of 8 cm^2) is only 15.28 mW (1.91 mW/cm$^2 \times$ 8 cm^2 = 15.28 mW), a simple estimation would indicate that the total generated electricity is 298.58 mW (100 mW/cm$^2 \times$ 11.85% $\times$ 25.2 cm^2 = 298.58 mW). Thus, there are 283.30 mW (298.58 mW – 15.28 mW = 283.30 mW) surplus energy could be stored in the ideal condition.

Moreover, the surplus energy collected and stored in ESS during the daytime is automatically switched to power the entire system at night with no extra energy input (**Fig. S19B**).

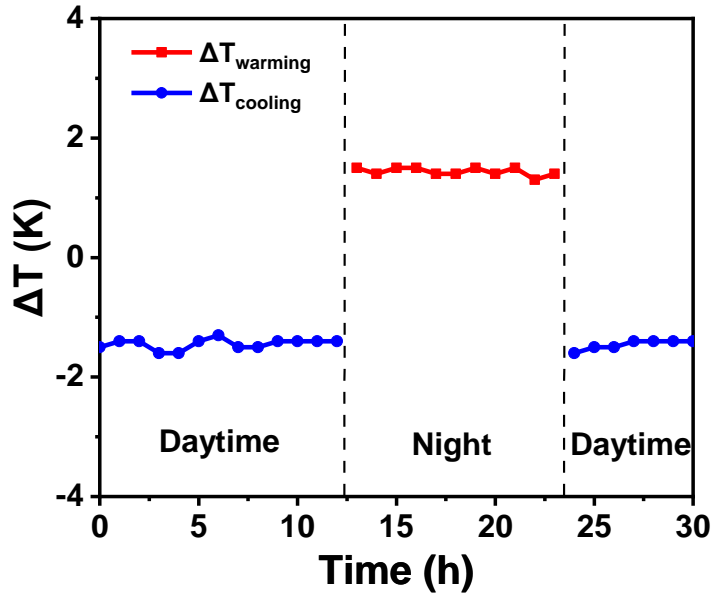## 20. Self-powered all-day thermoregulatory OETC system

Fig. S20. Performance of self-powered all-day thermoregulatory OETC system. The effective area of 25.2 cm^2 is required to achieve all-day thermoregulation. Operating for 12 h under the illumination intensity of 100 mW/cm^2 by solar simulator, the OETC can operate through all night using the storage energy during daytime.

In order to estimate the all-day thermoregulation of the OETC system, we used a simulated solar light source with a light intensity of 100 mW/cm^2 continuously irradiated on the OTEC system (25.2 cm^2 effective area of OPV module and 8 cm^2 effective area of EC thermoregulatory system) for 12 h, during which its cooling capacity was maintained at ~1.5 K (**Fig. S20**). Then, we turned off the solar simulator, and the OETC system automatically switched to heating mode. The energy stored in the ESS system was released and allowed the EC thermoregulatory system to continue operating for more than 12 h, during which its heating capacity remained at~1.5 K. The performance of the OETC system with sustainable self-powered all-day thermoregulation was achieved.

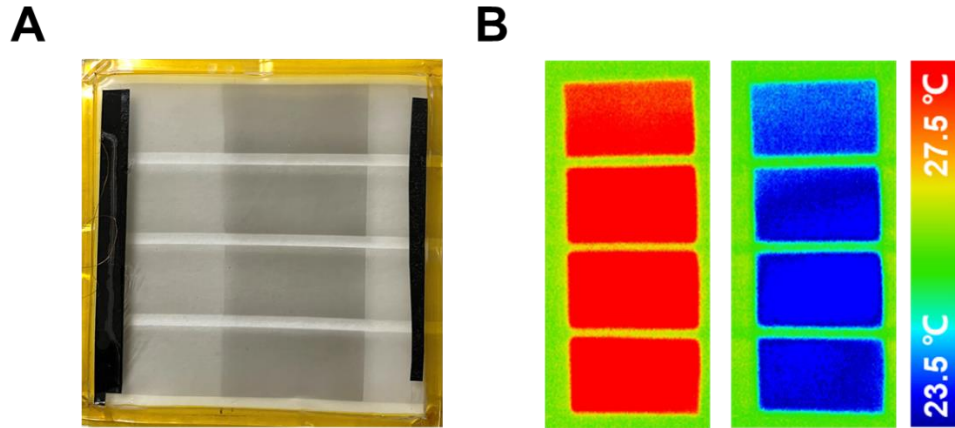**21. Four parallel EC arrays for simultaneous bidirectional thermoregulation**

Fig. S21. Thermoregulatory capacity of the EC polymer film arrays. (**A**) Four parallel EC film arrays (the total effective area is 4×8 cm^2). (**B**) Infrared thermal images of four parallel EC film arrays after application (left) and removal (right) electric field at the illumination intensity of 100 mW/cm^2.

To explicitly evaluate the thermoregulatory capacity of the EC polymer films driven by OPV module, we drove four effective areas of 2 cm $\times$ 4 cm parallel EC polymer film (**Fig. S21A**) using a flexible OPV module (effective area 25.2 cm^2, V_{oc} of 5.75 V, J_{sc} of 3.31 mA/cm^2, and P_{max} of 298.58 mW) under the light intensity of 100 mW/cm^2. It can be seen that the flexible OPV module can drive four active area arrays simultaneously for fast and effective cooling and heating (**Fig. S21B**) for efficient bidirectional thermoregulation under 100 mW/cm^2 light intensity.
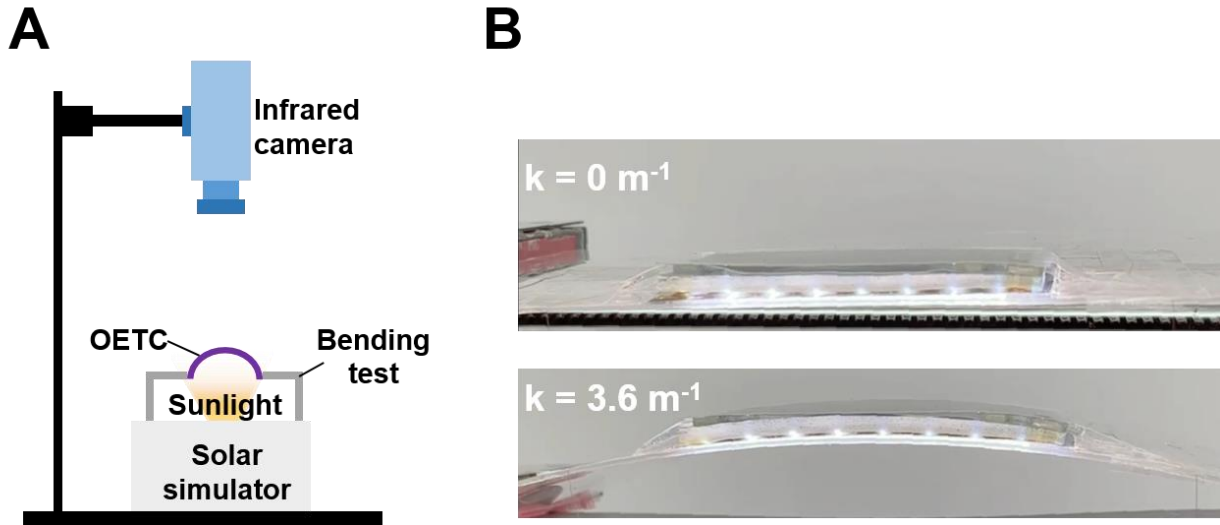
22. Bending measurement of OETC system

Fig. S22. Bending measurement of OETC system. (**A**) Schematic illustration of bending measuring system for thermoregulatory performance of OETC system. (**B**) Photographs of OETC in operation under different curvature (0 m^{-1} and 3.6 m^{-1}).

Fig. S22A shows the schematic illustration of bending measuring system of OETC system. During the bending test, the system is illuminated with 100 mW/cm^2 light at the bottom and its surface temperature is measured by infrared camera at the top. The maximum curvature of the whole system is up to 3.6 m^{-1} (**Fig. S22B**).

23. Thermoregulation of artificial skin with the initial temperature of 34 °C by the OETC under the illumination intensity of 100 mW/cm² by solar simulator at varying ambient temperatures.
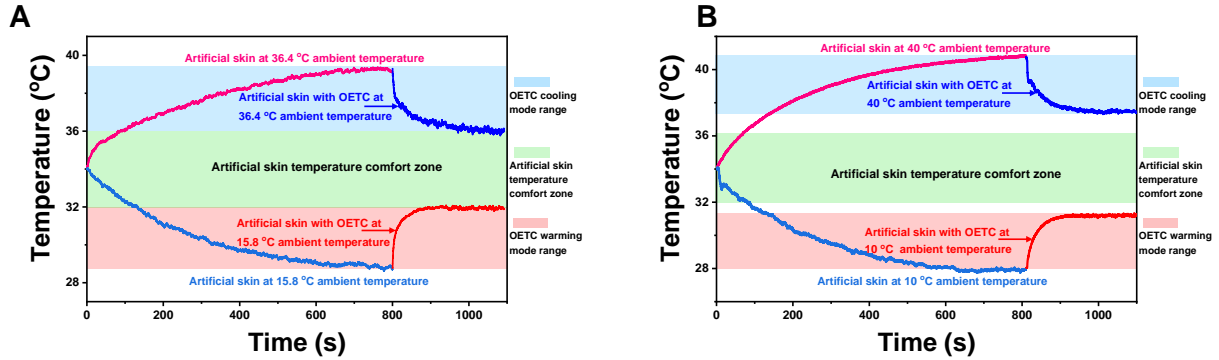

Fig. S23. Thermoregulation of artificial skin with the initial temperature of 34 °C by the OETC under the illumination intensity of 100 mW/cm² by solar simulator at varying ambient temperatures. (**A**) Thermoregulation of the artificial skin by the OETC under 15.8 °C and 36.4 °C ambient temperatures. (**B**) Thermoregulation of the artificial skin by the OETC under 10 °C and 40 °C ambient temperatures.

Fig. S23 shows thermoregulation of the artificial skin with the initial temperature of 34 °C by the OETC under the illumination intensity of 100 mW/cm² by solar simulator at varying ambient temperatures. When moving the skin into a low temperature environment at 15.8 °C, the artificial skin temperature almost drops to 28.8 °C (**Fig. S23A**), the OETC warming mode starts working, which raises the artificial skin temperature up to the thermal comfort zone of 32 °C. Correspondingly, while moving the skin into a high temperature environment at 36.4 °C, the artificial skin temperature almost increases to 39.3 °C. Then, the OETC cooling mode turns on, which brings the skin temperature drop to the thermal comfort zone of 36 °C. As a result, our OETC can maintain the artificial skin temperature within the thermal comfort zone between 32 and 36 °C (skin temperature), even though the environmental temperature varies between 15.8 to 36.4 °C with a large environmental temperature change of 20.6 K. Compared to bare artificial skin (4.0 K), OETC extends the thermal comfort zone of the artificial skin by 16.6 K (20.6 vs 4.0 K). Moreover, the skin can be warmed at a maximum rate of 18.8 °C/min or cooled at a maximum rate of 14.9 °C/min (calculated by the average temperature change rate in the first 5 s after operating

the OETC) to achieve fast thermoregulation when the ambient temperature is below or above the thermal comfort zone (**Fig. S23A**).

In addition, when the ambient temperature is too low such as at 10 °C or too high such as at 40 °C (**Fig. S23B**), OETC cannot restore the temperature of artificial skin to the thermal comfort zone. However, after the artificial skin is thermoregulated by the OETC, the temperature of artificial skin is close to thermal comfort zone. The OETC warming mode can raise the artificial skin temperature from 28.0 to 31.1 °C, while the OETC cooling mode could drop the artificial temperature from 40.8 to 37.4 °C.

Table S1. The performance of the OPV module under different illumination intensities from 55 to 100 mW/cm^2 by solar simulator.

I_{sun} (mW/cm^2)	V_{oc} (V)	J_{sc} (mA/cm^2)	FF (%)	Eff (%)	P_{max} (mW)
100	5.75	3.31	62.19	11.85	298.58
95	5.73	3.12	62.76	11.80	282.42
90	5.71	2.99	62.51	11.88	269.42
85	5.69	2.83	62.84	11.91	255.12
80	5.67	2.68	63.27	12.01	242.25
75	5.66	2.53	63.61	12.17	229.95
70	5.64	2.39	63.78	12.26	216.31
65	5.62	2.25	64.09	12.46	204.10
60	5.61	2.09	64.45	12.58	190.18
55	5.59	1.96	64.64	12.88	178.45

In **Table S1**, the large-area OPV module exhibits a promising PCE of 11.85% (V_{oc} of 5.75 V, J_{sc} of 3.31 mA/cm^2, FF of 62.19% and P_{max} of 298.58 mW) under illumination intensity of 100 mW/cm^2. Even at the low illumination intensity of 55 mW/cm^2, the V_{oc} of the module remains above 5.50 V and the P_{max} exceeds 170 mW, which ensures that the EC devices have sufficient voltage and power to drive continuously.

References and Notes

1. J. Chai, Z. Kang, Y. Yan, L. Lou, Y. Zhou, J. Fan, Thermoregulatory clothing with temperature-adaptive multimodal body heat regulation. *Cell Rep. Phys. Sci.* **3**, 100958 (2022). doi:10.1016/j.xcrp.2022.100958

2. ANSI/ASHRAE, *Standard 55: Thermal Environmental Conditions for Human Occupancy* (American Society of Heating, Refrigerating, and Air-Conditioning Engineers, 2017).

3. X. A. Zhang, S. Yu, B. Xu, M. Li, Z. Peng, Y. Wang, S. Deng, X. Wu, Z. Wu, M. Ouyang, Y. Wang, Dynamic gating of infrared radiation in a textile. *Science* **363**, 619–623 (2019). doi:10.1126/science.aau1217 Medline

4. S. Zeng, S. Pian, M. Su, Z. Wang, M. Wu, X. Liu, M. Chen, Y. Xiang, J. Wu, M. Zhang, Q. Cen, Y. Tang, X. Zhou, Z. Huang, R. Wang, A. Tunuhe, X. Sun, Z. Xia, M. Tian, M. Chen, X. Ma, L. Yang, J. Zhou, H. Zhou, Q. Yang, X. Li, Y. Ma, G. Tao, Hierarchical-morphology metafabric for scalable passive daytime radiative cooling. *Science* **373**, 692–696 (2021). doi:10.1126/science.abi5484 Medline

5. R. Xiao, C. Hou, W. Yang, Y. Su, Y. Li, Q. Zhang, P. Gao, H. Wang, Infrared-radiation-enhanced nanofiber membrane for sky radiative cooling of the human body. *ACS Appl. Mater. Interfaces* **11**, 44673–44681 (2019). doi:10.1021/acsami.9b13933 Medline

6. Q. Zhang, Y. Lv, Y. Wang, S. Yu, C. Li, R. Ma, Y. Chen, Temperature-dependent dual-mode thermal management device with net zero energy for year-round energy saving. *Nat. Commun.* **13**, 4874 (2022). [doi:10.1038/s41467-022-32528-1](doi:10.1038/s41467-022-32528-1) Medline

7. Q. Zhang, Y. Wang, Y. Lv, S. Yu, R. Ma, Bioinspired zero-energy thermal-management device based on visible and infrared thermochromism for all-season energy saving. *Proc. Natl. Acad. Sci. U.S.A.* **119**, e2207353119 (2022). doi:10.1073/pnas.2207353119 Medline

8. P.-C. Hsu, A. Y. Song, P. B. Catrysse, C. Liu, Y. Peng, J. Xie, S. Fan, Y. Cui, Radiative human body cooling by nanoporous polyethylene textile. *Science* **353**, 1019–1023 (2016). doi:10.1126/science.aaf5471 Medline

9. Y. Kou, K. Sun, J. Luo, F. Zhou, H. Huang, Z.-S. Wu, Q. Shi, An intrinsically flexible phase change film for wearable thermal managements. *Energy Storage Mater.* **34**, 508–514 (2021). doi:10.1016/j.ensm.2020.10.014

10. Z. Luo, D. Yang, J. Liu, H. Y. Zhao, T. Zhao, B. X. Li, W. G. Yang, Z. Z. Yu, Nature-inspired solar-thermal gradient reduced graphene oxide aerogel-based bilayer phase change composites for self-adaptive personal thermal management. *Adv. Funct. Mater.* **33**, 2212032 (2023). doi:10.1002/adfm.202212032

11. C. Wang, L. Hua, H. Yan, B. Li, Y. Tu, R. Wang, A thermal management strategy for electronic devices based on moisture sorption-desorption processes. *Joule* **4**, 435–447 (2020). doi:10.1016/j.joule.2019.12.005

12. J. A. Mason, J. Oktawiec, M. K. Taylor, M. R. Hudson, J. Rodriguez, J. E. Bachman, M. I. Gonzalez, A. Cervellino, A. Guagliardi, C. M. Brown, P. L. Llewellyn, N. Masciocchi, J. R. Long, Methane storage in flexible metal-organic frameworks with intrinsic thermal management. *Nature* **527**, 357–361 (2015). doi:10.1038/nature15732 Medline

13. L. Zhou, H. Song, N. Zhang, J. Rada, M. Singer, H. Zhang, B. S. Ooi, Z. Yu, Q. Gan, Hybrid concentrated radiative cooling and solar heating in a single system. *Cell Rep. Phys. Sci.* **2**, 100338 (2021). doi:10.1016/j.xcrp.2021.100338

14. H. Luo, Y. Zhu, Z. Xu, Y. Hong, P. Ghosh, S. Kaur, M. Wu, C. Yang, M. Qiu, Q. Li, Outdoor personal thermal management with simultaneous electricity generation. *Nano Lett.* **21**, 3879–3886 (2021). doi:10.1021/acs.nanolett.1c00400 Medline

15. L. Zhang, Q. Feng, J. Wang, J. Sun, X. Shi, X. Jiang, Microfluidic synthesis of rigid nanovesicles for hydrophilic reagents delivery. *Angew. Chem. Int. Ed.* **54**, 3952–3956 (2015). doi:10.1002/anie.201500096 Medline

16. M. Mokhtari Yazdi, M. Sheikhzadeh, Personal cooling garments: A review. *J. Text. Inst.* **105**, 1231–1250 (2014). [doi:10.1080/00405000.2014.895088](doi:10.1080/00405000.2014.895088)

17. M. Smith, V. Cacucciolo, H. Shea, Fiber pumps for wearable fluidic systems. *Science* **379**, 1327–1332 (2023). doi:10.1126/science.ade8654 Medline

18. G.-X. Li, T. Dong, L. Zhu, T. Cui, S. Chen, Microfluidic-blow-spinning fabricated sandwiched structural fabrics for all-season personal thermal management. *Chem. Eng. J.* **453**, 139763 (2023). [doi:10.1016/j.cej.2022.139763](doi:10.1016/j.cej.2022.139763)

19. Y. Guo, C. Dun, J. Xu, J. Mu, P. Li, L. Gu, C. Hou, C. A. Hewitt, Q. Zhang, Y. Li, D. L. Carroll, H. Wang, Ultrathin, washable, and large-area graphene papers for personal thermal management. *Small* **13**, 1702645 (2017). doi:10.1002/smll.201702645 Medline

20. Z. Guo, C. Sun, J. Wang, Z. Cai, F. Ge, High-performance laminated fabric with enhanced photothermal conversion and joule heating effect for personal thermal management. *ACS Appl. Mater. Interfaces* **13**, 8851–8862 (2021). doi:10.1021/acsami.0c23123 Medline

21. D. J. Silva, B. D. Bordalo, A. M. Pereira, J. Ventura, J. P. Araújo, Solid state magnetic refrigerator. *Appl. Energy* **93**, 570–574 (2012). doi:10.1016/j.apenergy.2011.12.002

22. Y. Liu, L. C. Phillips, R. Mattana, M. Bibes, A. Barthélémy, B. Dkhil, Large reversible caloric effect in FeRh thin films via a dual-stimulus multicaloric cycle. *Nat. Commun.* **7**, 11614 (2016). doi:10.1038/ncomms11614 Medline

23. S. Zhang, Q. Yang, C. Li, Y. Fu, H. Zhang, Z. Ye, X. Zhou, Q. Li, T. Wang, S. Wang, W. Zhang, C. Xiong, Q. Wang, Solid-state cooling by elastocaloric polymer with uniform chain-lengths. *Nat. Commun.* **13**, 9 (2022). [doi:10.1038/s41467-021-27746-y](doi:10.1038/s41467-021-27746-y) Medline

24. R. Wang, S. Fang, Y. Xiao, E. Gao, N. Jiang, Y. Li, L. Mou, Y. Shen, W. Zhao, S. Li, A. F. Fonseca, D. S. Galvão, M. Chen, W. He, K. Yu, H. Lu, X. Wang, D. Qian, A. E. Aliev, N. Li, C. S. Haines, Z. Liu, J. Mu, Z. Wang, S. Yin, M. D. Lima, B. An, X. Zhou, Z. Liu, R. H. Baughman, Torsional refrigeration by twisted, coiled, and supercoiled fibers. *Science* **366**, 216–221 (2019). doi:10.1126/science.aax6182 Medline

25. J. Choi, C. Dun, C. Forsythe, M. P. Gordon, J. J. Urban, Lightweight wearable thermoelectric cooler with rationally designed flexible heatsink consisting of phase-change material/graphite/silicone elastomer. *J. Mater. Chem. A Mater. Energy Sustain.* **9**, 15696–15703 (2021). [doi:10.1039/D1TA01911B](doi:10.1039/D1TA01911B)

26. H. Wei, J. Zhang, Y. Han, D. Xu, Soft-covered wearable thermoelectric device for body heat harvesting and on-skin cooling. *Appl. Energy* **326**, 119941 (2022). doi:10.1016/j.apenergy.2022.119941

27. Y. Zhang, J. Gao, S. Zhu, J. Li, H. Lai, Y. Peng, L. Miao, Wearable thermoelectric cooler based on a two-layer hydrogel/nickel foam heatsink with two-axis flexibility. *ACS Appl. Mater. Interfaces* **14**, 15317–15323 (2022). doi:10.1021/acsami.2c01777 Medline

28. R. A. Kishore, A. Nozariasbmarz, B. Poudel, M. Sanghadasa, S. Priya, Ultra-high performance wearable thermoelectric coolers with less materials. *Nat. Commun.* **10**, 1765 (2019). [doi:10.1038/s41467-019-09707-8](doi:10.1038/s41467-019-09707-8) Medline

29. R. Mutschler, M. Rüdisüli, P. Heer, S. Eggimann, Benchmarking cooling and heating energy demands considering climate change, population growth and cooling device uptake. *Appl. Energy* **288**, 116636 (2021). doi:10.1016/j.apenergy.2021.116636

30. L. Meng, Y. Zhang, X. Wan, C. Li, X. Zhang, Y. Wang, X. Ke, Z. Xiao, L. Ding, R. Xia, H.-L. Yip, Y. Cao, Y. Chen, Organic and solution-processed tandem solar cells with 17.3% efficiency. *Science* **361**, 1094–1098 (2018). doi:10.1126/science.aat2612 Medline

31. J. Wang, Z. Zheng, P. Bi, Z. Chen, Y. Wang, X. Liu, S. Zhang, X. Hao, M. Zhang, Y. Li, J. Hou, Tandem organic solar cells with 20.6% efficiency enabled by reduced voltage losses. *Natl. Sci. Rev.* **10**, nwad085 (2023). doi:10.1093/nsr/nwad085 Medline

32. G. Zeng, W. Chen, X. Chen, Y. Hu, Y. Chen, B. Zhang, H. Chen, W. Sun, Y. Shen, Y. Li, F. Yan, Y. Li, Realizing 17.5% efficiency flexible organic solar cells via atomic-level chemical welding of silver nanowire electrodes. *J. Am. Chem. Soc.* **144**, 8658–8668 (2022). doi:10.1021/jacs.2c01503 Medline

33. H. Jinno, K. Fukuda, X. Xu, S. Park, Y. Suzuki, M. Koizumi, T. Yokota, I. Osaka, K. Takimiya, T. Someya, Stretchable and waterproof elastomer-coated organic photovoltaics for washable electronic textile applications. *Nat. Energy* **2**, 780–785 (2017). [doi:10.1038/s41560-017-0001-3](doi:10.1038/s41560-017-0001-3)

34. A. Sharma, S. Masoumi, D. Gedefaw, S. O'Shaughnessy, D. Baran, A. Pakdel, Flexible solar and thermal energy conversion devices: Organic photovoltaics (OPVs), organic thermoelectric generators (OTEGs) and hybrid PV-TEG systems. *Appl. Mater. Today* **29**, 101614 (2022). doi:10.1016/j.apmt.2022.101614

35. R. Ma, Z. Zhang, K. Tong, D. Huber, R. Kornbluh, Y. S. Ju, Q. Pei, Highly efficient electrocaloric cooling with electrostatic actuation. *Science* **357**, 1130–1134 (2017). doi:10.1126/science.aan5980 Medline

36. Y. Bo, Q. Zhang, H. Cui, M. Wang, C. Zhang, W. He, X. Fan, Y. Lv, X. Fu, J. Liang, Y. Huang, R. Ma, Y. Chen, Electrostatic actuating double-unit electrocaloric cooling device with high efficiency. *Adv. Energy Mater.* **11**, 2003771 (2021). doi:10.1002/aenm.202003771

37. P. Bai, Q. Zhang, H. Cui, Y. Bo, D. Zhang, W. He, Y. Chen, R. Ma, An active pixel-matrix electrocaloric device for targeted and differential thermal management. *Adv. Mater.* **35**, e2209181 (2023). doi:10.1002/adma.202209181 Medline

38. H. Cui, Q. Zhang, Y. Bo, P. Bai, M. Wang, C. Zhang, X. Qian, R. Ma, Flexible microfluidic electrocaloric cooling capillary tube with giant specific device cooling power density. *Joule* **6**, 258–268 (2022). doi:10.1016/j.joule.2021.12.010

39. C.-Y. Liao, Y. Chen, C.-C. Lee, G. Wang, N.-W. Teng, C.-H. Lee, W.-L. Li, Y.-K. Chen, C.-H. Li, H.-L. Ho, P. H.-S. Tan, B. Wang, Y.-C. Huang, R. M. Young, M. R. Wasielewski, T. J. Marks, Y.-M. Chang, A. Facchetti, Processing strategies for an organic photovoltaic module with over 10% efficiency. *Joule* **4**, 189–206 (2020). doi:10.1016/j.joule.2019.11.006

40. S. Zhang, H. Chen, P. Wang, S. Li, Z. Li, Y. Huang, J. Liu, Z. Yao, C. Li, X. Wan, Y. Chen, A large area organic solar module with non-halogen solvent treatment, high efficiency, and decent stability. *Sol. RRL* **7**, 2300029 (2023). doi:10.1002/solr.202300029

41. See "Preparation of the flexible large-area OPV module" in the materials and methods for the detailed procedure.

42. B. Neese, B. Chu, S. G. Lu, Y. Wang, E. Furman, Q. M. Zhang, Large electrocaloric effect in ferroelectric polymers near room temperature. *Science* **321**, 821–823 (2008). doi:10.1126/science.1159655 Medline

43. Y. Meng, Z. Zhang, H. Wu, R. Wu, J. Wu, H. Wang, Q. Pei, A cascade electrocaloric cooling device for large temperature lift. *Nat. Energy* **5**, 996–1002 (2020). [doi:10.1038/s41560-020-00715-3](doi:10.1038/s41560-020-00715-3)

44. See "Preparation of the flexible EC device" in the materials and methods for the detailed procedure.

45. B. Dai, X. Li, T. Xu, X. Zhang, Radiative cooling and solar heating Janus films for personal thermal management. *ACS Appl. Mater. Interfaces* **14**, 18877–18883 (2022). doi:10.1021/acsami.2c01370 Medline

46. P.-C. Hsu, C. Liu, A. Y. Song, Z. Zhang, Y. Peng, J. Xie, K. Liu, C.-L. Wu, P. B. Catrysse, L. Cai, S. Zhai, A. Majumdar, S. Fan, Y. Cui, A dual-mode textile for human body radiative heating and cooling. *Sci. Adv.* **3**, e1700895 (2017). doi:10.1126/sciadv.1700895 Medline

47. F. Salata, I. Golasi, V. Ciancio, F. Rosso, Dressed for the season: Clothing and outdoor thermal comfort in the Mediterranean population. *Build. Environ.* **146**, 50–63 (2018). doi:10.1016/j.buildenv.2018.09.041

48. J. G. Metts, J. A. Nabity, D. M. Klaus, Theoretical performance analysis of electrochromic radiators for space suit thermal control. *Adv. Space Res.* **47**, 1256–1264 (2011). [doi:10.1016/j.asr.2010.11.018](doi:10.1016/j.asr.2010.11.018)

49. O. Montenbruck, P. Steigenberger, U. Hugentobler, Enhanced solar radiation pressure modeling for Galileo satellites. *J. Geod.* **89**, 283–297 (2014). [doi:10.1007/s00190-014-0774-0](doi:10.1007/s00190-014-0774-0)

50. See "Calculation of the required OPV module area to provide all-day thermoregulation for individual space travel" in the supplementary text for details.

51. G. Zhang, Q. Li, H. Gu, S. Jiang, K. Han, M. R. Gadinski, M. A. Haque, Q. Zhang, Q. Wang, Ferroelectric polymer nanocomposites for room-temperature electrocaloric refrigeration. *Adv. Mater.* **27**, 1450–1454 (2015). doi:10.1002/adma.201404591 Medline

52. A. Torelló, P. Lheritier, T. Usui, Y. Nouchokgwe, M. Gérard, O. Bouton, S. Hirose, E. Defay, Giant temperature span in electrocaloric regenerator. *Science* **370**, 125–129 (2020). doi:10.1126/science.abb8045 Medline

53. Y. Wang, Z. Zhang, T. Usui, M. Benedict, S. Hirose, J. Lee, J. Kalb, D. Schwartz, A high-performance solid-state electrocaloric cooling system. *Science* **370**, 129–133 (2020). doi:10.1126/science.aba2648 Medline

54. W. J. E. Beek, M. M. Wienk, M. Kemerink, X. Yang, R. A. J. Janssen, Hybrid zinc oxide conjugated polymer bulk heterojunction solar cells. *J. Phys. Chem. B* **109**, 9505–9516 (2005). doi:10.1021/jp050745x Medline

55. S. Li, Q. Fu, L. Meng, X. Wan, L. Ding, G. Lu, G. Lu, Z. Yao, C. Li, Y. Chen, Achieving over 18% efficiency organic solar cell enabled by a ZnO-based hybrid electron transport layer with an operational lifetime up to 5 years. *Angew. Chem. Int. Ed.* **61**, e202207397 (2022). doi:10.1002/anie.202207397 Medline

56. Y. Li, X. Huang, K. Ding, H. K. M. Sheriff Jr., L. Ye, H. Liu, C. Z. Li, H. Ade, S. R. Forrest, Non-fullerene acceptor organic photovoltaics with intrinsic operational lifetimes over 30 years. *Nat. Commun.* **12**, 5419 (2021). doi:10.1038/s41467-021-25718-w Medline

57. IEC 60479-1, "Effects of current on human beings and livestock— Part 1: General aspects," ed. 1.0 (2018).

58. G. Cilveli, A. Okur, V. Sülar, Electrostatic properties of clothing fabrics suitable for different end-uses. *Fibres Text. East. Eur.* **28**, 50–57 (2020). doi:10.5604/01.3001.0013.5858

59. G. Byagathvalli, S. Sinha, Y. Zhang, M. P. Styczynski, J. Standeven, M. Saad Bhamla, ElectroPen: An ultra-low-cost, electricity-free, portable electroporator. *PLOS Biol.* **18**, e3000589 (2020). doi:10.1371/journal.pbio.3000589 Medline